An X-ray investigation of the NGC 346 field in the SMC (2) : the field population

Y. Nazé[1,6], J.M. Hartwell[2], I.R. Stevens[2], J. Manfroid[1,7,8], S. Marchenko[3], M. F. Corcoran[4], A.F.J. Moffat[5] and G. Skalkowski[5]

ABSTRACT

We present results from a *Chandra* observation of the NGC 346 cluster, the ionizing source of N66, the most luminous H II region and the largest star formation region in the SMC. In the first part of this investigation, we have analysed the X-ray properties of the cluster itself and the remarkable star HD 5980. But the field contains additional objects of interest. In total, 79 X-ray point sources were detected in the *Chandra* observation and we investigate here their characteristics in details. The sources possess rather high HRs, and their cumulative luminosity function is steeper than the SMC's trend. Their absorption columns suggest that most of the sources belong to NGC 346. Using new *UBVRI* imaging with the ESO 2.2m telescope, we also discovered possible counterparts for 36 of these X-ray sources. Finally, some objects show X-ray and/or optical variability, and thus need further monitoring.

Subject headings: (galaxies:) Magellanic Clouds–X-rays: individual (NGC 346)

1. Introduction

The recent launch of the *Chandra* satellite provides an opportunity to explore the X-ray sky with a far greater sensitivity and spatial resolution than ever before. In a given field of interest, these characteristics enable the discovery of numerous X-ray sources in addition of the main target(s). Often regarded as secondary, these sources provide however important informations which can improve our knowledge of the X-ray emission mechanisms in the Universe.

We have obtained a deep *Chandra* observation of the giant H II region N66 (Henize 1956), the largest star formation region in the SMC. The large number of massive stars and the presence of the remarkable star HD 5980 make the NGC 346 field one of the best opportunities to conduct an investigation of the X-ray domain.

In the first part of this analysis (Nazé et al., paper I), we have presented the characteristics of the cluster, the star HD 5980 and its close neighbourhood. The cluster itself was relatively faint and most of its emission seemed correlated with the location of the brightest stars in the core. However, the level of X-ray emission could not be explained solely by the emission from individual stars. The *Chandra* observation also provides the first detection of HD 5980. In X-rays, the star, that underwent a LBV-type eruption in 1994, ap-

[1]Institut d'Astrophysique et de Géophysique, Université de Liège, Allée du 6 Août 17, Bat. B5c, B 4000 - Liège (Belgium); naze@astro.ulg.ac.be, manfroid@astro.ulg.ac.be

[2]School of Physics & Astronomy, University of Birmingham, Edgbaston, Birmingham B15 2TT (UK); jmh@star.sr.bham.ac.uk, irs@star.sr.bham.ac.uk

[3]Department of Physics and Astronomy, Thompson Complex Central Wing, Western Kentucky University, Bowling Green, KY 42101-3576; sergey@astro.wku.edu

[4]Universities Space Research Association, High Energy Astrophysics Science Archive Research Center, Goddard Space Flight Center, Greenbelt, MD 20771; corcoran@barnegat.gsfc.nasa.gov

[5]Département de physique, Université de Montreal, C.P. 6128, Succ. Centre-Ville, Montreal, QC, H3C 3J7 (Canada); moffat@astro.umontreal.ca, gwen@astro.umontreal.ca

[6]Research Fellow F.N.R.S.

[7]Research Director F.N.R.S.

[8]Visiting Astronomer, European Southern Observatory

pears very bright, comparable only to the brightest WR stars in the Galaxy. This high luminosity could be explained either by colliding winds in the binary system or by post-eruption effects. Finally, a bright, extended X-ray emission seems to surround this star. It is probably due to a SNR which may or may not be related to HD 5980 itself (see paper I).

In this second paper, we will focus on the other X-ray sources present in the field. First, we will describe in § 2 the observations used in this study. The detected sources, their HRs, and their spectral characteristics will then be discussed in § 3, 4, and 5, respectively. Next, we will describe the overall properties of the point sources' population in § 6, present their possible counterparts in § 7 and investigate their variability in § 8. Finally, we will conclude in § 9.

2. The Observations and Data Analysis

2.1. X-ray observations

NGC 346 was observed with *Chandra* for the XMEGA[9] consortium on 2001 May 15–16 for 100 ks (98.671 ks effective, ObsID = 1881, JD~2 452 045.2d). The data were recorded by the ACIS-I0, I1, I2, I3, S2 and S3 CCD chips maintained at a temperature of -120°C. The data were taken with a frame time of 3.241s in the faint mode. Our faintest sources have fluxes of about 2×10^{32} erg s^{-1} (see §6.), assuming a distance of 59 kpc for the SMC. More details about the processing of the data can be found in paper I.

For long exposures, removing the afterglow events can adversely affect the science analysis (underestimation of the fluxes, alteration of the spectra and so on). We thus computed a new level 2 events file and we will use this new file throughout this paper, except for the source detection, where it is better to use the pipeline level 2 product to avoid mistaking afterglow events for real sources.

Further analysis was performed using the CIAO v2.1.2 software provided by the CXC and also with the FTOOLS tasks. The spectra were analysed and fitted within XSPEC v11.0.1 (Arnaud 1996). Fig. 1 shows an image of the four ACIS-I chips : numerous point sources and some diffuse emission near HD 5980 can be seen.

[9]http://lheawww.gsfc.nasa.gov/users/corcoran/xmega/xmega.html

2.2. WFI images

The photometric data have been acquired as part of a project aiming at the photometric calibration of the Optical Monitor onboard the ESA satellite *XMM-Newton* (Mason et al. 2001). The NGC 346 field was among the selected fields observed by *XMM-Newton* that were photometrical, calibrated on the basis of ground-based observations.

The images of this field were obtained in April 2001 at the MPG/ESO 2.2-m telescope with the WFI mosaic camera providing a field of view of 0.5×0.5 square degrees. Due to the unfavorable position of the SMC at this period of the year, the seeing was less than perfect but the data quality was still good. The total exposures times were 25 minutes in the U-band and about 10 minutes in the other bands ($BVRI$). The reductions were performed with IRAF and our personal software. Color transformations were done via observations of standard Landolt fields.

3. Source Detection and Count Rate

The discrete X-ray sources of the field were first found by running the CIAO wavelet algorithm *wavdetect* on an unbinned image of each chip. The source detection threshold was set to 5×10^{-7}, implying that a maximum of one false source would be detected within each chip. A total of 68 sources were then found: 7 sources in ACIS-I0, 19 sources in ACIS-I1, 16 sources in ACIS-I2, 23 sources in ACIS-I3 and 3 sources in ACIS-S3. A simpler source detection algorithm was also used: using statistical thresholds calculated after Gehrels (1986), the algorithm searched significant events on separated soft, medium and hard energy bands images. In addition of the 68 sources already detected, it found 11 complementary ones. We present in Table 1 the coordinates of all these sources, listed by increasing Right Ascension (RA). Fig. 1 shows the sources' positions

on the ACIS-I chips. Note that HD 5980 is designated our Src 47 and that Src 50, belonging most probably to the extended emission, probably does not constitute in itself a distinct point source. One source, Src 36, was 'detected' in the emission associated to the NGC 346 cluster. This emission was analysed in paper I. Some other sources are very faint, or are situated near a CCD gap and their derived properties should therefore be treated with caution.

Table 1 also lists the count rates of each source in the $0.3 - 10.0$ keV energy band. The count rate was derived from a spatial extraction of counts in a disk centered on the detected source, using the tool *dmextract*. The background was extracted in an annulus surrounding the source. The analysis of the ACIS-S3 sources was more difficult. Src 6 and 7 are too close to be deblended and to extract individual count rates for each source. Only a global rate was then extracted: $2.38 \pm 0.06 \times 10^{-2}$ cnts s^{-1}. Src 3 also seems to possess a close neighbor (although this one was not detected by the detection algorithm), preventing the extraction of an individual count rate for Src 3: the global count rate for the region encompassing Src 3 and its possible neighbour is $2.77 \pm 0.08 \times 10^{-2}$ cnts s^{-1}. A comparison with the PSF expected at this position on the ACIS-I detector confirms that it is not a single source.

Although the detection algorithm did not find any sources on the ACIS-S2 chip and only 3 on the ACIS-S3 chip (Src 3, 6 and 7), at least three additional sources on these chips are detected by eye. Due to the high background of these CCDs, however, we will not analyse any of these further. We have listed these additional sources (and their approximate centroids) in Table 1 as Src 80, 81 and 82.

4. Hardness Ratios

The properties of the point sources have been studied using their hardness ratios (HRs). As in Sarazin, Irwin, & Bergman (2001) and Blanton, Sarazin, & Irwin (2001), we have defined S, M and H as the count rates in the $0.3 - 1.0$ keV, $1.0 - 2.0$ keV and $2.0 - 10.0$ keV energy bands. We then used these data to compute two HRs: $H21$ is defined as $(M - S)/(M + S)$ and $H31$ as $(H - S)/(H + S)$. For the brightest sources (with more than 50 cnts, i.e., a count rate of minimum 5×10^{-4} cnts s^{-1}), the S, M and H count rates are listed with the corresponding HRs in Table 2. Fig. 2 shows $H31$ as a function of $H21$ for these sources. No supersoft source is present, and the sources seem generally quite hard: the HRs extend mainly from $(0,0)$ to $(1,1)$, with a tight correlation between the two HRs. The harder character of the sources in the NGC 346 field, as compared to NGC 4697 (Sarazin, Irwin, & Bergman 2001) and NGC 1553 (Blanton, Sarazin, & Irwin 2001), can be explained by the larger absorbing column.

5. Spectral Fitting

We have extracted the spectra of the detected point sources using the CIAO tool *psextract*. As in the previous section, only sources with at least 50 cnts were fully analysed. Models were fitted within XSPEC, and we used either a simple absorbed *mekal* model or an absorbed power-law model, whose properties are summarized in Table 3. Unfortunately, the low Signal-to-Noise of most spectra did not allow us to discriminate between the models, so we have listed the parameters of both models, except if they give unphysical results (e.g. $kT > 10$ keV) or a statistically poor fit to the data. If neither model fits the data, other models were tested, and we have listed the parameters of the best one. Unless otherwise stated, the abundances of the *mekal* models were always fixed to the SMC mean value, $0.1 Z_{\odot}$.

5.1. Absorption column

To better understand the spectral properties of the point sources, we have tried to estimate the absorption column, $N(H)$. We can use two different ways. First, the HI surveys provide us direct estimations of the neutral hydrogen column: Schwering & Israel (1991) gives 4.3×10^{20} cm^{-2} for the Galactic N(HI), Mc Gee & Newton (1982) have measured neutral hydrogen columns in the range $(3.7 - 5.3) \times 10^{21}$ cm^{-2} towards NGC 346 and Israel (1997) quotes 4.4×10^{21} cm^{-2} for $N(H_2)$ towards NGC 346.

The value of the absorbing column should then be $\sim N(\mathrm{HI})_{\mathrm{gal}}$ for sources located in front of the SMC, $N(\mathrm{HI})_{\mathrm{gal}} + \mathrm{N(HI)}_{\mathrm{NGC\,346}} + 2\mathrm{N(H_2)}_{\mathrm{NGC\,346}}$ for extragalactic sources, and intermediate values for sources within the SMC.

A second estimation of the extinction towards NGC 346 can be made using the reddening, $E(B-V)$. Massey, Parker & Garmany (1989) measured an average $E(B-V)$ of 0.14 mag in the cluster, and Schwering & Israel (1991) estimate the Galactic contribution to 0.07 to 0.09 mag. We can convert these values to absorption columns using the gas-to-dust ratios. For the Galaxy, this ratio is estimated to be $[N(\mathrm{HI})/\mathrm{E(B-V)}]_{\mathrm{gal}} = 5.8 \times 10^{21}$ cm^{-2} mag^{-1} (Bohlin, Savage, & Drake 1978). For the SMC, the quoted values are in the range $[N(\mathrm{HI})/\mathrm{E(B-V)}]_{\mathrm{SMC}} = (3.7-8.7) \times 10^{22}$ cm^{-2} mag^{-1} (Bouchet et al. 1985; Lequeux et al. 1994; Fitzpatrick 1985). A range of typical absorption columns towards NGC 346 can then be calculated using the expression $ratio_{gal}E(B-V)_{gal} + ratio_{NGC\,346}E(B-V)_{NGC\,346}$.

We can thus conclude that an absorption column in the $4 - 20 \times 10^{20}$ cm^{-2} range indicates most probably a source in front of NGC 346 but still belonging to the SMC, while a column in the $2 - 6 \times 10^{21}$ cm^{-2} is characteristic of a source situated in the NGC 346 cluster. A column higher than $\sim 10^{22}$ cm^{-2} rather suggests an extragalactic source. An histogram of the values of the absorbing columns found in our spectral fits is presented in Fig. 3. It shows that most sources are indeed situated in NGC 346, with only few foreground sources (e.g. the extended X-ray emission surrounding HD 5980) and at most one third of extragalactic sources.

6. Point Source Luminosity Function

We have used the X-ray luminosities of all the point sources detected in the field to construct a luminosity function, which can be compared to the overall luminosity function of the SMC, as well as to other galaxies. We already know the luminosities of the brightest sources, thanks to their spectral analysis (see Table 3). However, we need to estimate the luminosities of the fainter sources on the basis of their count rate only.

To determine a representative count-to-luminosity conversion, we have assumed that all sources lie in the SMC, at a distance of 59 kpc. We have extracted a cumulative spectrum of all fainter sources, excluding those with large errors (those that are faint or near a CCD gap). This cumulative spectrum was best fitted by an absorbed power law with $N(H) = 0.52 \times 10^{22}$ cm^{-2} and Γ=1.66. Note that this value of the absorbing column is comparable to that estimated for sources belonging to the cluster in § 5.1. For these parameters, $PIMMS$[10] gave us a typical absorbed flux of 1.3990×10^{-11} erg cm^{-2} s^{-1} cnts^{-1} in the 0.3 – 10.0 keV energy band, leading to a count-to-luminosity conversion factor of 5.8281×10^{36} erg s^{-1} cnts^{-1}. The derived absorbed luminosities for the fainter sources are listed in Table 1.

Using these luminosities, we have constructed the cumulative distribution of the sources as a function of luminosity (see Fig. 4). The best fit power law to our data, using a χ^2 minimisation algorithm, possesses an exponent of -1.02 (with a 90% confidence range of -0.98 to -1.06). For comparison, Bauer et al. (2001) indicate that the typical trend of the luminosity function for the SMC, M82 and NGC 3256 (all of which are star-forming galaxies of varying size) is $N \propto L_X^{-0.65}$ for $L_X > 10^{34}$ erg s^{-1}. The fit suggests that these data show a rather steeper luminosity function than for is seen the entire SMC at higher luminosities, and also other star-forming galaxies. Note however, that in these observations we are sampling a lower luminosity range than in these other examples.

7. Source Identification

7.1. Comparison with previous X-ray observations

We have compared our source list to the *ROSAT* and *ASCA* catalogs of the SMC X-ray sources (Haberl et al. 2000). Only 15 of the 82

[10] available on http://asc.harvard.edu/toolkit/pimms.jsp

sources were previously detected. We give in Table 4 the correspondence between our sources and the previously detected ones. To be complete, we also quoted in this table the distance between our source and the *ROSAT/ASCA* detections, and the 90% confidence error on the position given in the catalogs.

Of these 15 sources, Src 3, 13, 24, 77, 78 and 79 fall slightly beyond the allowed range of RA and DEC of their *ROSAT* counterpart[11]. Either the quoted errors were underestimated, or there are six pairs of close transient sources in the field, with one member in a high state and the other in a quiescent state when the *ROSAT* observation was taken, and then exactly the reverse situation when *Chandra* took our data. As this possibility is very unlikely, we prefer to accept the identification with the quoted *ROSAT* sources.

During this comparison, we also found that one previously detected source was clearly missing: [HFP2000] 186 (Haberl et al. 2000). [HFP2000] 186 (quoted in *Simbad* with a O7III counterpart even if it is very close to a B-type star, AzV 219[12]), is not far from our Src 41, but still at a distance of 56″, to be compared with the quoted positional error on this *ROSAT* source, 22″. This source may be a transient X-ray binary (XRB). Another *ROSAT* source, [HFP2000] 202, should be present in the ACIS-S2 field, but is not detected clearly.

7.2. Optical counterparts

To search for optical counterparts, we have used the *DSS* and *MACHO* databases. In addition, we have also compared the X-ray data to ground-based images taken with the Wide Field Imager (WFI). The limiting magnitudes are $R \sim 17.5$ mag for the *DSS*, 20-21 mag for MACHO and ~21 mag for WFI. Before the comparison with the WFI images, a global shift of 0.3s in RA and 1.2″ in DEC was first applied to the coordinates of our sources, so that the position of HD 5980 coincides almost perfectly in both datasets.

Next we have defined an optical counterpart as a star lying less than 3″ away from the position of the X-ray source. The results of this search are listed in the last column of Table 1. 36 sources possess at least one counterpart within the chosen 3″ error circle, but some of these counterparts are faint and/or lying just at the 3″ border. 18 other sources do not seem to present any counterpart in any of the datasets. The status of the rest of the sources is unclear: they present a faint counterpart in some of the optical images, but not in all of them, so we considered these identifications more dubious than the previous ones. In Table 5, we present the *UBVRI* photometry of the counterparts found in the WFI data, and their distance from the X-ray source (after that the first global shift has been applied, see above). Fig. 5 presents the color-magnitude diagram of these sources.

Among the identified sources, the slightly extended X-ray source Src 2 corresponds in fact to a small cluster of stars, too close to each other to disentangle their individual X-ray emission. A bright optical source is found located between Src 6 and 7 (which are located on the ACIS-S3 chip): it is possible that these two sources in fact be only one source corresponding to this bright star. The two X-ray sources are ~ 8″ apart, but the spatial resolution of *Chandra* is substantially degraded this far off-axis.

Src 9 and 78 are known Be/X-ray binaries (Be/XRBs). We confirm here the previous identifications of Src 9 with [MA93] 1038[13] (Haberl & Sasaki 2000) and Src 78 with a 15-16th magnitude star (Kahabka & Pietsch 1996). Haberl & Sasaki (2000) found another Be/XRB candidate in our field: [HFP2000] 170 (our Src 5). It is lying between the emission-line stars AzV 191 and [MA93] 1016. The precise position of this source on the *ROSAT* observations made the association with either star unlikely, and we found that this source correlates well with a faint star situated between these two bright emission-line stars.

[11] This is also true for the *ROSAT* sources observed on ACIS-S, but as all parameters derived for these sources are highly uncertain, we will not argue this point further.

[12] AzV stars come from the catalog by Azzopardi, Vigneau, & Macquet (1975)

[13] [MA93] stars come from the catalog by Meyssonnier & Azzopardi (1993)

8. Variability

8.1. Short-term Variability

We have searched for short-term X-ray variability in the brightest point sources (with > 50 cnts). Using a Kolmogorov-Smirnov test, we found that all lightcurves are consistent with a constant flux at >95 % confidence level. However, KS tests are not very sensitive, so we have also checked the (non-)variability using χ^2 tests. We have compared the χ^2 of a constant fit with the χ^2 of a linear fit, and we have detected a significant improvement when using the linear fits for Src 5, 9, and 47 (=HD 5980, see paper I), suggesting that these sources are indeed variable. Fig. 6a and b show the lightcurves of Src 5 and 9, respectively. Src 5 and 47 present an increase of the count rate towards the end of the exposure, but the variability of Src 9 seems more complex and may be related to the Be phenomenon (see § 7.2.)

Considering even higher frequency variability, Lamb et al. (2002) have detected a period of ~5 s in Src 77, the brightest point source of the field, which presents ~6000 counts in 100 ks. On basis of its luminosity and its soft spectrum, they have proposed it to be an Anomalous X-ray Pulsar (AXP). Using our photometry and a mean reddening of E(B-V)=0.14 mag (Massey, Parker & Garmany 1989), we can classify the counterpart as a probable early B star. This suggests that the source could be in fact an Be/X-ray binary. From the P_{orb} vs P_{pulsar} diagram (Corbet 1986), we then derived an orbital period of ~25 days.

8.2. Long-term Variations

Long-term variations in the X-ray properties can also be checked by comparing our *Chandra* data to the *ROSAT* PSPC observations of the SMC. We have already mentioned (§ 7.1.) one *ROSAT* source which was not detected in our *Chandra* observation. Such variations are indicative of transient sources.

One transient source was already known in this field: Src 78. Kahabka & Pietsch (1996) reveal that this source is an X-ray binary evolving from 1.3×10^{36} erg s^{-1} in the high state to $< 4.6 \times 10^{34}$ erg s^{-1} six months later. In our dataset, this source is in the quiescent state, since its luminosity reaches only 2×10^{34} erg s^{-1}. We have used the *ROSAT* data to compare the spectral properties of this source during the high and low states. The best fit parameters to the *ROSAT* observation of Src 78 in the high state are: $N(H) = 0.39^{0.68}_{0.17} \times 10^{22}$ cm^{-2} and $\Gamma = 2.82^{4.22}_{1.68}$. The flux in the 0.3 – 2.0 keV band was 5.03×10^{-13} erg cm^{-2} s^{-1} in October 1991, two orders of magnitude larger than the flux in the same band in May 2001 ($\sim 5 \times 10^{-15}$ erg cm^{-2} s^{-1}). The variations of the spectrum of Src 78 can be seen in Fig. 7a. Such luminosity variations were also observed in other sources, e.g. 2E0050.1 – 7247, but in this last case, the power-law steepened when the source luminosity decreased (Israel et al. 1997). However, if we consider only the *Chandra* data in the *ROSAT* energy range (0.3 – 2.0 keV), the fitted slopes of the power-laws are very similar in both datasets, thus we can not conclude whether the power-law has steepened or not. On the other hand, this X-ray source possesses a variable counterpart in the visible wavelengths. Fig. 7b shows the MACHO light curve of this star in the blue and red filters, binned to 25 days. Both curves show a long-term increase, superposed on a sinusoidal variation with a period of 1361 days. The properties of this interesting varying object are certainly worth further investigation.

We have also compared *Chandra* and *ROSAT* data in the 0.3 – 2.0 keV range for the other bright sources detected by *ROSAT*. The spectral properties from the *ROSAT* data of these sources are compatible with *Chandra* data within the error bars.

In addition, we can note that some of the X-ray sources may possess a variable optical counterpart. Using the MACHO database we found some long-term variables that correspond to our X-ray sources. They are presented in Table 6, along with the periods found (if any). Except for Src 78, no variation was clearly detected for these sources in the X-ray data, but future X-ray observations could provide additional checks.

9. Summary

In this serie of articles, we report the analysis of the *Chandra* data of N66, the largest star formation region of the SMC. In the first paper, we have presented the characteristics of the X-ray emission from the cluster's core and HD 5980. We have also discussed the nature and properties of the extended emission apparently surrounding HD 5980.

In this second article, we have focused on the other sources detected in the field. The X-ray properties of 79 point sources, of which 36 may possess an optical counterpart, have been analysed. Considering their absorption column, most of these sources probably belong to NGC 346. They show a rather hard spectra and their cumulative luminosity function appears steeper than the global one of the SMC. Due to their variability, some sources should be monitored in the future, both in the visible and X-ray ranges.

REFERENCES

Arnaud, K. 1996, ASP Conf. Ser. 101, eds G. Jacoby & J. Barnes, p.17

Azzopardi, M., Vigneau, J., & Macquet, M. 1975, A&AS, 22, 285 (AzV)

Bauer, F.E., Brandt, W.N., Sambruna, R.M., Chartas, G., Garmire, G.P., Kaspi, S., & Netzer, H. 2001, AJ, 122, 182

Blanton, E.L., Sarazin, C.L., & Irwin, J.A. 2001 ApJ, 552, 106

Bohlin, R.C., Savage, B.D., & Drake, J.F. 1978, ApJ, 224, 132

Bouchet, P., Lequeux, J., Maurice, E., Prevot, L., & Prevot-Burnichon, M.L. 1978, A&A, 149, 330

Corbet, R.H.D. 1986, MNRAS, 220, 1047

Fitzpatrick, E.L. 1985, ApJS, 59, 77

Gehrels, N. 1986, ApJ, 303, 336

Haberl, F., Filipovic, M. D., Pietsch, W., & Kahabka, P. 2000, A&AS, 142, 41 (HFP2000)

Haberl, F., & Sasaki, M. 2000, A&A 359, 573

Henize, K.G. 1956, ApJS, 2, 315

Irwin, J.A., Sarazin, C.L., & Bregman, J.N. 2002, ApJ, submitted (astro-ph/0107493)

Israel, G.L., Stella, L., Angelini, L., White, N.E., Giommi, P., & Covino, S. 1997, ApJ, 484, L141

Israel, F.P. 1997, A&A, 328, 471

Kahabka, P., & Pietsch, W. 1996, A&A, 312, 919

Lamb, R.C., Fox, D.W., Macomb, D.J., & Prince, T.A. 2002, submitted (astro-ph/0205310)

Lejeune, T. & Schaerer, D. 2001, A&A, 366, 538

Lequeux, J., Le Bourlot, J., Des Forets, G.P., Roueff, E., Boulanger, F., & Rubio, M. 1994, A&A, 292, 371

Mc Gee, R.X. & Newton, L.M. 1982, PASA, 4, 308

Mason, K.O., Breeveld, A., Much, R., Carter, M., Cordova, F.A., Cropper, M.S., Fordham, J., Huckle, H., Ho, C., Kawakami, H., Kennea, J., Kennedy, T., Mittaz, J., Pandel, D., Priedhorsky, W.C., Sasseen, T., Shirey, R., Smith, P., & Vreux, J.-M. 2001, A&A, 365, L36

Massey, P., Parker, J.W., & Garmany, C.D. 1989, AJ, 98, 1305

Mathewson, D.S., Ford, V.L., & Visvanathan, N. 1986, ApJ 301, 664

Meyssonnier, N., & Azzopardi, M. 1993, A&AS, 102, 451 (MA93)

Nazé et al., in preparation (paper I)

Sarazin, C.L., Irwin, J.A., & Bergman, J.N. 2001, ApJ, 556, 533

Schwering, P.B.W. & Israel, F.P. 1991, A&A, 246, 231

This 2-column preprint was prepared with the AAS LaTeX macros v5.0.

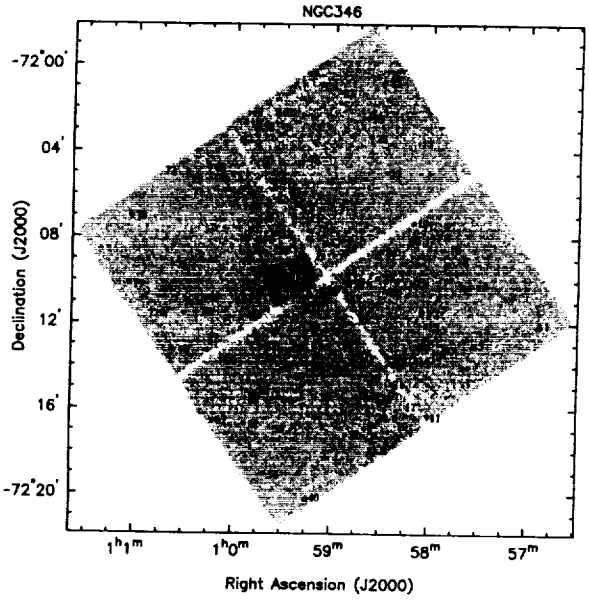

Fig. 1.— The NGC 346 field as seen by the *Chandra* ACIS-I. The image has been adaptively smoothed. The identification numbers of the sources found in the ACIS-I data of NGC 346 are shown (see Table 1 for a list of positions). The NGC 346 cluster corresponds to Src 36 and HD 5980 is Src 47. A cross has been used to show the location of faint sources. Note, that a number of point sources were located on the ACIS-S3 chip and are not shown in this diagram (Srcs 3, 6 and 7 and also src 80, 81 and 82 - see text for more details).

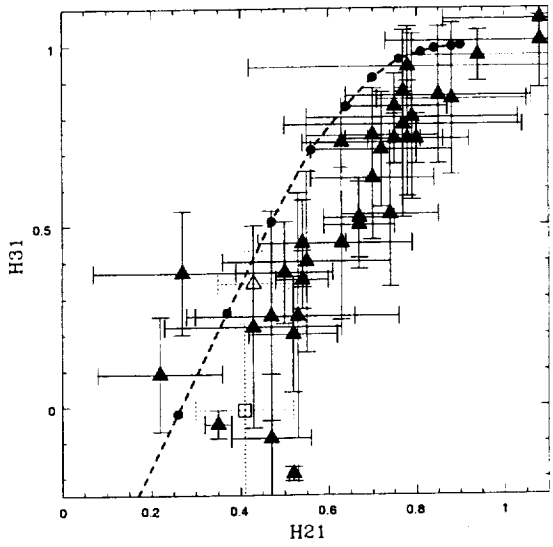

Fig. 2.— Hardness ratios of the brightest sources (those with a total of > 50 counts). The NGC 346 cluster is shown as an open square and HD 5980 as an open triangle (see paper I). The dots connected by a dashed line represents the colors predicted from an absorbed power-law model with a column density of 0.52×10^{22} cm^{-2} (see § 6.) and an exponent Γ varying from 0 (upper right) to 4.0 in increments of 0.4 (Irwin, Sarazin, & Bregman 2002). The extended emission surrounding HD 5980 is not shown on the diagram, being very soft, with $H21 = -0.24 \pm 0.02$ and $H31 = -0.96 \pm 0.05$.

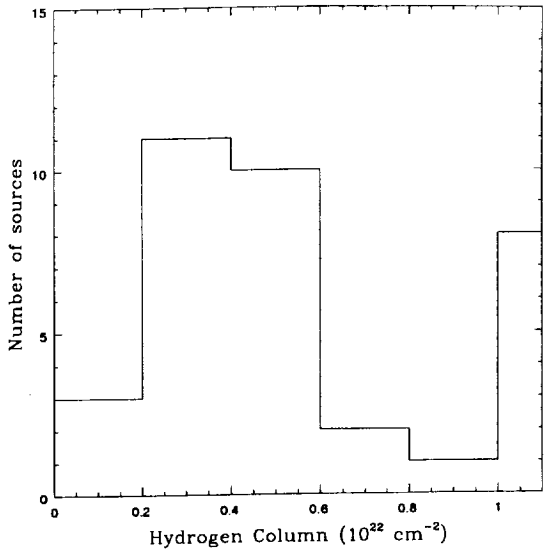

Fig. 3.— Histogram of the different values of the absorbing column $N(H)$ found for the point sources from the spectral fitting. Sources with a column of $\sim 2 - 6 \times 10^{21}$ cm^{-2} are probably associated with NGC 346, while those sources with $N(H) \geq 10^{22}$ cm^{-2} are likely to be extragalactic in nature.

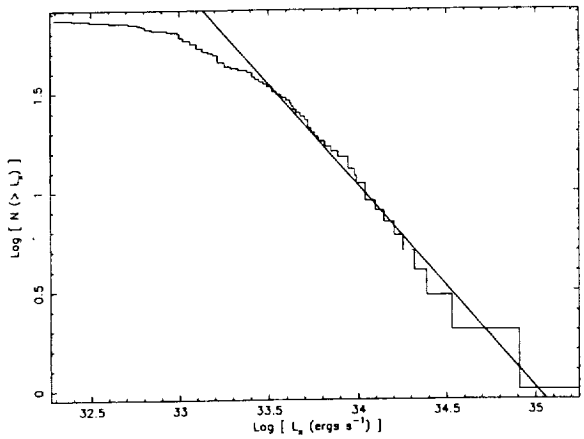

Fig. 4.— Histogram of the cumulative X-ray luminosity function of all the detected sources versus $0.3 - 10.0$ keV luminosity. The continuous line is the best-fit power law to the data (for $\log(L_X)>33.4$), which has a slope of $\alpha = -1.02$. The low luminosity data have not been used for the fit, since they are likely to be affected by incompleteness.

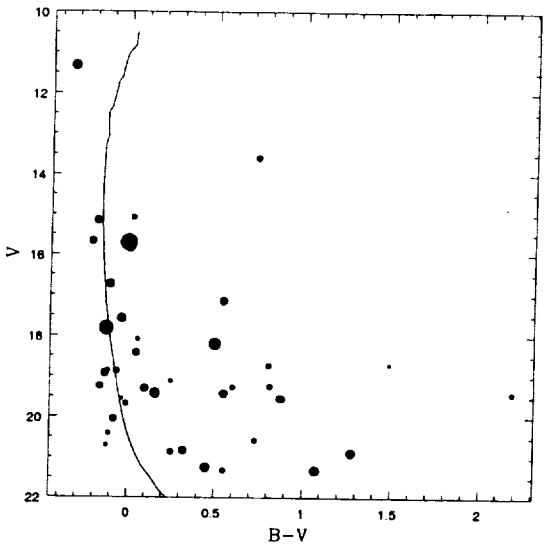

Fig. 5.— The Color-Magnitude Diagram for the sources listed in Table 5. The size of the dot is proportional to $\log(L_X)$. The solid line shows an isochrone of 5 Myr for Z=0.2 $Z_\odot$ (Lejeune & Schaerer 2001) transformed using a distance modulus of 18.85 mag and reddened with a R_V=3.3 and a E(B-V) of 0.14 mag (Massey, Parker & Garmany 1989).

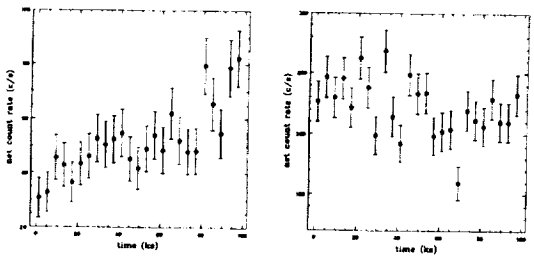

Fig. 6.— The *Chandra* X-ray lightcurve of Src 5 (a) and Src 9 (b), in the 0.3-10 keV range and with 25 bins of 4 ks each.

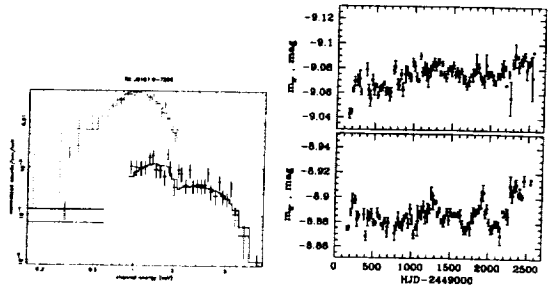

Fig. 7.— a. Variations of the spectrum of Src 78: The *ROSAT* data (shown with a lighter grey) extend over a smaller energy range than the *Chandra* data, but show a substantially increased luminosity. The models superimposed on the data are absorbed power-laws with $N_{H\,ROSAT}$ = 0.39 × 10^{22} cm^{-2}, Γ_{ROSAT}=2.82, $N_{H\,Chandra}$ = 0.36 × 10^{22} cm^{-2}, $\Gamma_{Chandra}$=1.01. b. MACHO light curve of the optical counterpart to Src 67 in the blue and red filters, binned to 25 days.

Table 1: Coordinates of all detected sources with their individual count rate and luminosities in the 0.3 – 10.0 keV band (see § 6.). The errors on the coordinates are given in sec for the right ascension (RA) and in $''$ for the declination (DEC). The last two columns indicates if the source is variable (see § 8) and if it posesses an optical counterpart (see § 7.2.). A counterpart is defined as lying within $\sim 3''$ away from the position of the X-ray source. An '?' status was attributed when a faint counterpart was detected at the position, but only in one of the optical images.

Src	RA (2000)	DEC (2000)	Count Rate	Luminosities	Var. ?	Co. ?
	hh mm ss ± *ss*	° ′ ″ ± ″	cnts s^{-1}	erg s^{-1}		
1	00 56 52.178±0.037	−72 12 03.80 ± 0.25	$2.65\pm0.22\times10^{-3}$	see Table 3	N	?
2	00 57 12.904±0.048	−72 10 43.25 ± 0.19	$8.41\pm1.18\times10^{-4}$	see Table 3	N	Y
3	00 57 17.991±0.027	−72 25 29.25 ± 0.14	see §3.			N
4	00 57 30.060±0.070	−72 10 09.20 ± 0.32	$2.93\pm0.90\times10^{-4}$	$1.71\pm0.52\times10^{33}$		?
5	00 57 32.411±0.012	−72 13 01.41 ± 0.06	$1.31\pm0.04\times10^{-2}$	see Table 3	Y	Y
6	00 57 34.782±0.021	−72 19 29.90 ± 0.10	see §3.			Y
7	00 57 36.269±0.023	−72 19 34.09 ± 0.08	see §3.			Y
8	00 57 41.568±0.043	−72 09 02.59 ± 0.23	$7.57\pm1.17\times10^{-4}$	see Table 3	N	?
9	00 57 50.041±0.004	−72 07 54.96 ± 0.03	$5.60\pm0.08\times10^{-2}$	see Table 3	Y	Y
10	00 57 51.162±0.055	−72 08 27.75 ± 0.39	$2.13\pm0.71\times10^{-4}$	$1.24\pm0.41\times10^{33}$		N
11	00 57 59.561±0.071	−72 16 19.18 ± 0.23	$6.36\pm1.14\times10^{-4}$	see Table 3	N	?
12	00 58 00.323±0.041	−72 08 22.01 ± 0.22	$2.77\pm0.70\times10^{-4}$	$1.61\pm0.41\times10^{33}$		Y
13	00 58 02.309±0.031	−72 12 05.68 ± 0.13	$1.57\pm0.15\times10^{-3}$	see Table 3	N	?
14	00 58 07.265±0.073	−72 13 48.43 ± 0.23	$1.76\pm0.66\times10^{-4}$	$1.03\pm0.38\times10^{33}$		Y
15	00 58 08.409±0.047	−72 03 36.98 ± 0.33	$8.01\pm1.23\times10^{-4}$	see Table 3	N	N
16	00 58 09.066±0.022	−72 08 25.62 ± 0.15	$1.01\pm0.12\times10^{-3}$	see Table 3	?	N
17	00 58 09.370±0.070	−72 16 12.20 ± 0.32	$4.66\pm1.22\times10^{-4}$	$2.72\pm0.71\times10^{33}$		N
18	00 58 11.883±0.052	−72 07 18.94 ± 0.41	$2.34\pm0.69\times10^{-4}$	$1.36\pm0.40\times10^{33}$		?
19	00 58 13.540±0.070	−72 16 13.80 ± 0.32	$4.74\pm4.47\times10^{-5}$	$2.76\pm2.61\times10^{32}$		?
20	00 58 19.900±0.070	−72 16 17.80 ± 0.32	$1.76\pm0.76\times10^{-4}$	$1.03\pm0.44\times10^{33}$		Y
21	00 58 22.688±0.042	−72 14 48.48 ± 0.31	$1.65\pm0.68\times10^{-4}$	$9.62\pm3.93\times10^{32}$		?
22	00 58 27.126±0.019	−72 10 24.68 ± 0.16	$3.24\pm0.71\times10^{-4}$	$1.89\pm0.41\times10^{33}$		N
23	00 58 27.453±0.027	−72 04 57.36 ± 0.17	$1.57\pm0.15\times10^{-3}$	see Table 3	N	N
24	00 58 30.043±0.011	−72 08 39.98 ± 0.05	$2.23\pm0.17\times10^{-3}$	see Table 3	N	Y
25	00 58 30.370±0.070	−72 00 44.60 ± 0.32	$6.80\pm1.25\times10^{-4}$	see Table 3	N	N
26	00 58 30.687±0.039	−72 15 28.36 ± 0.18	$5.44\pm0.98\times10^{-4}$	$3.17\pm0.57\times10^{33}$		Y
27	00 58 31.478±0.024	−72 09 50.62 ± 0.10	$4.49\pm0.79\times10^{-4}$	$2.62\pm0.46\times10^{33}$		?
28	00 58 37.336±0.020	−72 03 21.95 ± 0.11	$4.34\pm0.23\times10^{-3}$	see Table 3	N	?
29	00 58 37.753±0.071	−72 14 35.71 ± 0.23	$2.48\pm0.78\times10^{-4}$	$1.45\pm0.46\times10^{33}$		N
30	00 58 39.386±0.034	−72 02 27.15 ± 0.27	$1.02\pm0.13\times10^{-3}$	see Table 3	N	?
31	00 58 40.583±0.031	−72 10 01.69 ± 0.09	$5.75\pm4.12\times10^{-5}$	$3.35\pm2.40\times10^{32}$		N
32	00 58 49.750±0.070	−72 17 14.90 ± 0.32	$2.99\pm0.98\times10^{-4}$	$1.74\pm0.57\times10^{33}$		Y
33	00 58 58.200±0.070	−72 01 07.40 ± 0.32	$1.08\pm0.69\times10^{-4}$	$6.29\pm4.02\times10^{32}$		Y
34	00 59 00.744±0.008	−72 13 28.75 ± 0.04	$3.18\pm0.19\times10^{-3}$	see Table 3	N	Y
35	00 59 03.105±0.007	−72 12 22.80 ± 0.03	$3.06\pm0.19\times10^{-3}$	see Table 3	N	N
36	00 59 04.165±0.039	−72 10 23.25 ± 0.15	in the cluster's core, see paper I			Y

Table 1: (continued)

37	00 59 08.135±0.020	−72 12 45.85 ± 0.10	$1.12\pm0.47\times10^{-4}$	$6.53\pm2.76\times10^{32}$		?
38	00 59 08.915±0.084	−72 15 31.01 ± 0.22	$1.72\pm0.65\times10^{-4}$	$1.00\pm0.38\times10^{33}$		?
39	00 59 11.273±0.041	−72 12 23.61±0.16	$1.01\pm0.50\times10^{-4}$	$5.89\pm2.90\times10^{32}$		?
40	00 59 12.490±0.070	−72 20 11.70±0.32	$4.36\pm1.06\times10^{-4}$	$2.54\pm0.62\times10^{33}$		Y
41	00 59 13.042±0.045	−72 16 17.80±0.12	$1.14\pm0.13\times10^{-3}$	see Table 3	N	Y
42	00 59 18.146±0.024	−72 11 14.90±0.10	$2.84\pm0.70\times10^{-4}$	$1.66\pm0.41\times10^{33}$		?
43	00 59 18.826±0.041	−72 04 23.55±0.26	$7.33\pm1.10\times10^{-4}$	see Table 3	N	Y
44	00 59 21.780±0.050	−72 15 40.12±0.19	$2.37\pm0.68\times10^{-4}$	$1.38\pm0.40\times10^{33}$		Y
45	00 59 24.748±0.059	−72 12 42.98±0.21	$3.85\pm4.67\times10^{-5}$	$2.24\pm2.72\times10^{32}$		Y
46	00 59 25.365±0.039	−72 14 31.47±0.12	$7.93\pm1.04\times10^{-4}$	see Table 3	N	?
47	00 59 26.247±0.010	−72 09 52.66±0.04	$2.98\pm0.19\times10^{-3}$	see Table 3	Y	Y
48	00 59 29.589±0.034	−72 12 34.65±0.17	$1.12\pm0.47\times10^{-4}$	$6.53\pm2.76\times10^{32}$		?
49	00 59 31.434±0.024	−72 14 17.24±0.11	$1.34\pm0.13\times10^{-3}$	see Table 3	N	?
50	00 59 33.762±0.042	−72 10 39.72±0.19	$3.20\pm1.24\times10^{-4}$	$1.87\pm0.72\times10^{33}$		N
51	00 59 33.972±0.018	−72 07 48.36±0.09	$9.77\pm1.16\times10^{-4}$	see Table 3	N	Y
52	00 59 34.776±0.038	−72 02 10.73±0.20	$1.79\pm0.17\times10^{-3}$	see Table 3	N	Y
53	00 59 35.223±0.022	−72 08 35.08±0.10	$3.99\pm0.79\times10^{-4}$	$2.33\pm0.46\times10^{33}$		?
54	00 59 36.543±0.042	−72 08 07.16±0.17	$8.11\pm4.50\times10^{-5}$	$4.73\pm2.62\times10^{32}$		N
55	00 59 36.925±0.068	−72 16 52.46±0.17	$5.67\pm1.06\times10^{-4}$	see Table 3	N	Y
56	00 59 40.232±0.075	−72 19 03.24±0.15	$1.10\pm0.14\times10^{-3}$	see Table 3	N	?
57	00 59 42.910±0.045	−72 13 06.94±0.15	$2.06\pm0.73\times10^{-4}$	$1.20\pm0.43\times10^{33}$		Y
58	00 59 46.214±0.048	−72 02 51.73±0.33	$6.13\pm1.10\times10^{-4}$	see Table 3	N	N
59	00 59 46.617±0.054	−72 15 14.29±0.28	$9.71\pm7.44\times10^{-5}$	$5.66\pm4.34\times10^{32}$		Y
60	00 59 47.340±0.027	−72 09 29.51±0.12	$2.16\pm0.62\times10^{-4}$	$1.26\pm0.36\times10^{33}$		?
61	00 59 49.632±0.044	−72 10 20.14±0.21	$1.93\pm0.62\times10^{-4}$	$1.12\pm0.36\times10^{33}$		Y
62	00 59 52.006±0.064	−72 16 40.39±0.33	$1.69\pm0.69\times10^{-4}$	$9.85\pm4.00\times10^{32}$		N
63	00 59 52.542±0.051	−72 15 30.39±0.14	$9.32\pm1.14\times10^{-4}$	see Table 3	N	?
64	00 59 53.254±0.054	−72 06 34.00±0.21	$4.49\pm0.87\times10^{-4}$	$2.62\pm0.51\times10^{33}$		Y
65	00 59 54.300±0.048	−72 10 31.79±0.18	$1.82\pm0.62\times10^{-4}$	$1.06\pm0.36\times10^{33}$		Y
66	01 00 06.170±0.070	−72 13 44.00±0.32	$1.28\pm0.64\times10^{-4}$	$7.46\pm3.73\times10^{32}$		N
67	01 00 11.742±0.087	−72 16 29.06±0.21	$2.84\pm0.83\times10^{-4}$	$1.66\pm0.48\times10^{33}$		Y
68	01 00 15.509±0.036	−72 04 41.21±0.17	$2.64\pm0.20\times10^{-3}$	see Table 3	?	Y
69	01 00 17.138±0.053	−72 10 50.07±0.20	$4.91\pm0.89\times10^{-4}$	$2.86\pm0.52\times10^{33}$		Y
70	01 00 22.994±0.033	−72 11 28.73±0.15	$1.26\pm0.14\times10^{-3}$	see Table 3	?	N
71	01 00 28.081±0.055	−72 05 33.30±0.22	$7.73\pm1.43\times10^{-4}$	see Table 3	N	?
72	01 00 28.460±0.070	−72 04 51.50±0.32	$2.25\pm0.83\times10^{-4}$	$1.31\pm0.48\times10^{33}$		?
73	01 00 29.039±0.055	−72 05 12.33±0.26	$6.03\pm1.33\times10^{-4}$	see Table 3	N	Y
74	01 00 30.126±0.071	−72 11 29.14±0.18	$2.23\pm0.66\times10^{-4}$	$1.30\pm0.38\times10^{33}$		N
75	01 00 36.740±0.070	−72 09 13.60±0.32	$3.45\pm0.87\times10^{-4}$	$2.01\pm0.51\times10^{33}$		?
76	01 00 36.919±0.058	−72 13 16.33±0.20	$9.32\pm1.29\times10^{-4}$	see Table 3	?	Y
77	01 00 42.828±0.007	−72 11 32.36±0.02	$6.06\pm0.08\times10^{-2}$	see Table 3	N	Y
78	01 01 02.620±0.041	−72 06 57.54±0.19	$2.92\pm0.20\times10^{-3}$	see Table 3	Y	Y
79	01 01 03.898±0.046	−72 10 04.96±0.16	$1.80\pm0.16\times10^{-3}$	see Table 3	N	Y
80	00 56 40.263±0.988	−72 17 00.94±4.58	additional source, see §3.			
81	00 56 41.920±0.960	−72 20 27.43±4.51	additional source, see §3.			
82	00 57 23.203±2.944	−72 23 56.39±13.0	additional source, see §3.			

Table 2: Count rates in the S, M and H energy bands, and derived hardness ratios.

Src	S cnts s^{-1}	M cnts s^{-1}	H cnts s^{-1}	$H21$	$H31$
1	$3.81\pm0.99\times10^{-4}$	$1.26\pm0.14\times10^{-3}$	$1.00\pm0.15\times10^{-3}$	0.54 ± 0.10	0.45 ± 0.12
2	$1.72\pm0.58\times10^{-4}$	$2.97\pm0.75\times10^{-4}$	$3.72\pm0.83\times10^{-4}$	0.27 ± 0.20	0.37 ± 0.17
5	$3.27\pm0.20\times10^{-3}$	$6.85\pm0.28\times10^{-3}$	$2.95\pm0.19\times10^{-3}$	0.35 ± 0.03	-0.05 ± 0.04
8	$1.11\pm0.57\times10^{-4}$	$3.87\pm0.78\times10^{-4}$	$2.59\pm0.82\times10^{-4}$	0.55 ± 0.19	0.40 ± 0.25
9	$2.39\pm0.17\times10^{-3}$	$1.87\pm0.04\times10^{-2}$	$3.50\pm0.06\times10^{-2}$	0.77 ± 0.02	0.87 ± 0.01
11	$1.17\pm0.52\times10^{-4}$	$3.25\pm0.75\times10^{-4}$	$1.94\pm0.84\times10^{-4}$	0.47 ± 0.19	0.25 ± 0.29
13	$2.54\pm0.69\times10^{-4}$	$7.55\pm1.01\times10^{-4}$	$5.57\pm0.97\times10^{-4}$	0.50 ± 0.11	0.37 ± 0.14
15	$2.70\pm4.15\times10^{-5}$	$4.29\pm0.81\times10^{-4}$	$3.45\pm0.94\times10^{-4}$	0.88 ± 0.17	0.85 ± 0.21
16	$9.12\pm4.45\times10^{-5}$	$6.18\pm0.90\times10^{-4}$	$2.97\pm0.71\times10^{-4}$	0.74 ± 0.11	0.53 ± 0.20
23	$8.26\pm4.52\times10^{-5}$	$5.86\pm0.90\times10^{-4}$	$9.04\pm1.15\times10^{-4}$	0.75 ± 0.12	0.83 ± 0.09
24	$2.43\pm0.64\times10^{-4}$	$1.21\pm0.12\times10^{-3}$	$7.75\pm1.04\times10^{-4}$	0.67 ± 0.08	0.52 ± 0.11
25	$1.34\pm0.55\times10^{-4}$	$3.37\pm0.85\times10^{-4}$	$2.09\pm0.87\times10^{-4}$	0.43 ± 0.20	0.22 ± 0.28
26	$-1.02\pm2.65\times10^{-5}$	$2.60\pm0.64\times10^{-4}$	$2.94\pm0.78\times10^{-4}$	1.08 ± 0.22	1.07 ± 0.19
28	$6.69\pm1.01\times10^{-4}$	$2.27\pm0.17\times10^{-3}$	$1.40\pm0.15\times10^{-3}$	0.54 ± 0.06	0.35 ± 0.08
30	$7.73\pm4.93\times10^{-5}$	$4.78\pm0.85\times10^{-4}$	$4.63\pm0.94\times10^{-4}$	0.72 ± 0.16	0.71 ± 0.16
34	$2.13\pm0.59\times10^{-4}$	$1.52\pm0.14\times10^{-3}$	$1.44\pm0.13\times10^{-3}$	0.75 ± 0.06	0.74 ± 0.07
35	$1.82\pm0.54\times10^{-4}$	$1.67\pm0.14\times10^{-3}$	$1.21\pm0.12\times10^{-3}$	0.80 ± 0.06	0.74 ± 0.07
41	$8.44\pm4.68\times10^{-5}$	$4.73\pm0.85\times10^{-4}$	$5.84\pm0.93\times10^{-4}$	0.70 ± 0.15	0.75 ± 0.13
43	$2.70\pm3.96\times10^{-5}$	$3.33\pm0.71\times10^{-4}$	$3.73\pm0.86\times10^{-4}$	0.85 ± 0.21	0.86 ± 0.19
46	$9.90\pm4.77\times10^{-5}$	$4.30\pm0.78\times10^{-4}$	$2.64\pm0.65\times10^{-4}$	0.63 ± 0.16	0.45 ± 0.21
47	$5.34\pm0.90\times10^{-4}$	$1.35\pm0.13\times10^{-3}$	$1.09\pm0.12\times10^{-3}$	0.43 ± 0.08	0.34 ± 0.09
49	$1.33\pm3.41\times10^{-5}$	$4.14\pm0.78\times10^{-4}$	$9.10\pm1.13\times10^{-4}$	0.94 ± 0.16	0.97 ± 0.07
51	$-0.60\pm2.68\times10^{-5}$	$1.64\pm0.54\times10^{-4}$	$8.19\pm1.06\times10^{-4}$	1.08 ± 0.35	1.01 ± 0.07
52	$3.14\pm0.76\times10^{-4}$	$1.00\pm0.12\times10^{-3}$	$4.73\pm1.05\times10^{-4}$	0.52 ± 0.10	0.20 ± 0.16
55	$9.51\pm5.59\times10^{-5}$	$3.12\pm0.71\times10^{-4}$	$1.60\pm0.71\times10^{-4}$	0.53 ± 0.23	0.25 ± 0.34
56	$7.09\pm4.75\times10^{-5}$	$5.61\pm0.92\times10^{-4}$	$4.70\pm1.02\times10^{-4}$	0.78 ± 0.14	0.74 ± 0.16
58	$3.34\pm4.16\times10^{-5}$	$2.81\pm0.73\times10^{-4}$	$2.98\pm0.84\times10^{-4}$	0.79 ± 0.24	0.80 ± 0.23
63	$8.44\pm4.49\times10^{-5}$	$4.73\pm0.82\times10^{-4}$	$3.75\pm0.78\times10^{-4}$	0.70 ± 0.14	0.63 ± 0.17
68	$2.92\pm0.84\times10^{-4}$	$1.48\pm0.14\times10^{-3}$	$8.75\pm1.38\times10^{-4}$	0.67 ± 0.08	0.50 ± 0.12
70	$3.36\pm0.79\times10^{-4}$	$5.28\pm0.89\times10^{-4}$	$4.00\pm0.94\times10^{-4}$	0.22 ± 0.14	0.09 ± 0.16
71	$4.62\pm5.95\times10^{-5}$	$3.51\pm0.84\times10^{-4}$	$3.76\pm1.14\times10^{-4}$	0.77 ± 0.27	0.78 ± 0.26
73	$-5.73\pm5.52\times10^{-5}$	$3.81\pm0.87\times10^{-4}$	$2.80\pm1.00\times10^{-4}$	1.35 ± 0.41	1.51 ± 0.66
76	$2.36\pm4.17\times10^{-5}$	$1.89\pm0.64\times10^{-4}$	$7.20\pm1.13\times10^{-4}$	0.78 ± 0.36	0.94 ± 0.11
77	$1.24\pm0.04\times10^{-2}$	$3.98\pm0.06\times10^{-2}$	$8.36\pm0.31\times10^{-3}$	0.52 ± 0.01	-0.19 ± 0.02
78	$2.50\pm0.72\times10^{-4}$	$1.09\pm0.12\times10^{-3}$	$1.58\pm0.15\times10^{-3}$	0.63 ± 0.09	0.73 ± 0.07
79	$3.88\pm0.81\times10^{-4}$	$1.09\pm0.12\times10^{-3}$	$3.24\pm0.92\times10^{-4}$	0.47 ± 0.09	-0.09 ± 0.18

Table 3: Parameters of the spectral fits. Stated errors correspond to the 90 % confidence level. Abundances are fixed at $0.1Z_{\odot}$, except for src 77, where the best fit is found for $Z = 0.0022^{0.0094}_{0.0001}Z_{\odot}$. Luminosities are given in the spectral range 0.3 – 10 keV and for a distance of 59 kpc.

Src	Model	Luminosity (ergs s^{-1})	χ^2_ν	$N(H)$ (10^{22} cm^{-2})	Other parameters (kT in keV)	N_{dof}
1	wabs*mekal	1.65×10^{34}	0.81	$0.29^{0.49}_{0.15}$	$kT = 9.37^{55.75}_{4.56}$	29
	wabs*pow	1.72×10^{34}	0.82	$0.36^{0.57}_{0.21}$	Γ=$1.65^{1.98}_{1.32}$	29
2	wabs*pow	5.62×10^{33}	1.55	$0.20^{0.48}_{0.00}$	Γ=$1.31^{2.07}_{0.71}$	7
5	wabs*(mekal+ wabs*mekal)	4.42×10^{34}	1.03	$0.34^{0.73}_{0.22}$	kT_1=$0.27^{0.63}_{0.17}$ N_{H2}=$0.00^{0.10}_{0.00}$ kT_2=$3.03^{3.78}_{2.29}$	94
8	wabs*mekal	4.21×10^{33}	0.40	$0.24^{0.64}_{0.02}$	$kT = 8.48^{100.00}_{2.37}$	8
	wabs*pow	4.50×10^{33}	0.42	$0.30^{0.81}_{0.05}$	Γ=$1.64^{2.57}_{1.00}$	8
9	wabs*(mekal+ wabs*pow)	5.25×10^{35}	1.52	$1.02^{1.20}_{0.89}$	$kT = 0.58^{0.65}_{0.49}$ N_{H2}=$0.87^{1.64}_{0.17}$ Γ=$1.20^{1.37}_{1.10}$	314
11	wabs*mekal	2.87×10^{33}	1.22	$0.51^{0.80}_{0.02}$	$kT = 4.88^{100.00}_{1.59}$	6
	wabs*pow	3.15×10^{33}	1.23	$0.36^{1.20}_{0.02}$	Γ=$1.91^{3.53}_{1.07}$	6
13	wabs*pow	1.00×10^{34}	0.91	$0.16^{0.34}_{0.04}$	Γ=$1.50^{1.94}_{1.18}$	14
15	wabs*mekal	4.14×10^{33}	0.69	$0.92^{1.60}_{0.53}$	$kT = 3.12^{8.98}_{1.56}$	7
	wabs*pow	4.37×10^{33}	0.58	$1.19^{2.06}_{0.71}$	Γ=$2.49^{3.70}_{1.65}$	7
16	wabs*mekal	4.62×10^{33}	0.52	$0.52^{0.80}_{0.27}$	$kT = 2.88^{8.08}_{1.69}$	7
	wabs*pow	5.17×10^{33}	0.35	$0.67^{1.12}_{0.44}$	Γ=$2.34^{3.19}_{1.81}$	7
23	wabs*mekal	9.47×10^{33}	1.86	$1.39^{2.13}_{0.74}$	$kT = 5.52^{100.00}_{2.04}$	14
	wabs*pow	9.58×10^{33}	1.78	$1.80^{2.89}_{0.87}$	Γ=$2.21^{3.16}_{1.68}$	14
24	wabs*mekal	9.21×10^{33}	0.30	$0.50^{0.65}_{0.35}$	$kT = 3.68^{6.60}_{2.57}$	19
	wabs*pow	1.00×10^{34}	0.24	$0.64^{0.91}_{0.48}$	Γ=$2.18^{2.40}_{1.85}$	19
25	wabs*mekal	3.53×10^{33}	0.73	$0.18^{0.50}_{0.00}$	$kT = 7.52^{100.0}_{1.64}$	8
	wabs*pow	3.71×10^{33}	0.71	$0.25^{0.70}_{0.00}$	Γ=$1.73^{3.07}_{0.89}$	8
28	wabs*mekal	2.22×10^{34}	1.10	$0.19^{0.27}_{0.12}$	$kT = 7.43^{16.60}_{4.52}$	39
	wabs*pow	2.32×10^{34}	1.06	$0.26^{0.36}_{0.19}$	Γ=$1.75^{1.92}_{1.52}$	39
30	wabs*mekal	4.37×10^{33}	1.21	$1.19^{1.86}_{0.44}$	$kT = 2.45^{6.25}_{1.25}$	8
	wabs*pow	4.75×10^{33}	1.11	$1.55^{2.83}_{0.76}$	Γ=$2.76^{4.47}_{2.16}$	8
34	wabs*pow	1.85×10^{34}	0.94	$0.54^{0.73}_{0.39}$	Γ=$1.64^{1.86}_{1.38}$	29
35	wabs*mekal	1.42×10^{34}	0.61	$0.57^{0.74}_{0.44}$	$kT = 4.24^{6.66}_{3.63}$	25
	wabs*pow	1.50×10^{34}	0.61	$0.74^{0.95}_{0.57}$	Γ=$2.16^{2.30}_{1.82}$	25

Table 3: (continued)

41	wabs*pow	6.17×10^{33}	1.82	$0.39^{1.84}_{0.20}$	$\Gamma=1.57^{1.84}_{1.21}$	10
43	wabs*pow	5.21×10^{33}	0.17	$0.59^{1.16}_{0.39}$	$\Gamma=1.49^{2.53}_{1.09}$	7
46	wabs*mekal	3.28×10^{33}	0.96	$0.41^{0.92}_{0.20}$	$kT=4.24^{12.24}_{1.96}$	5
	wabs*pow	3.46×10^{33}	1.00	$0.56^{1.00}_{0.24}$	$\Gamma=2.11^{3.14}_{1.60}$	5
47	wabs*mekal	1.30×10^{34}	1.24	$0.22^{0.35}_{0.14}$	$kT=7.04^{13.35}_{4.35}$	27
	wabs*pow	1.36×10^{34}	1.30	$0.28^{0.44}_{0.19}$	$\Gamma=1.74^{1.89}_{1.53}$	27
49	wabs*mekal	9.29×10^{33}	1.40	$1.78^{1.09}_{2.74}$	$kT=5.70^{18.48}_{2.35}$	12
	wabs*pow	9.71×10^{33}	1.32	$2.12^{3.75}_{1.23}$	$\Gamma=2.09^{2.77}_{1.64}$	12
51	wabs*pow	1.18×10^{34}	1.05	$1.83^{4.55}_{0.72}$	$\Gamma=1.01^{2.52}_{0.13}$	7
52	wabs*mekal	6.67×10^{33}	1.26	$0.39^{0.58}_{0.26}$	$kT=2.60^{4.47}_{1.29}$	17
	wabs*pow	7.15×10^{33}	1.23	$0.56^{0.82}_{0.41}$	$\Gamma=2.51^{3.10}_{2.09}$	17
55	wabs*mekal	3.26×10^{33}	1.05	$0.25^{0.56}_{0.01}$	$kT=5.16^{72.88}_{1.87}$	6
	wabs*pow	3.58×10^{33}	1.12	$0.30^{0.71}_{0.02}$	$\Gamma=1.83^{2.79}_{1.14}$	6
56	wabs*pow	7.29×10^{33}	1.27	$0.37^{0.78}_{0.17}$	$\Gamma=1.52^{2.22}_{1.06}$	13
58	wabs*mekal	3.90×10^{33}	1.16	$0.96^{2.71}_{0.29}$	$kT=4.27^{100.00}_{1.23}$	7
	wabs*pow	4.29×10^{33}	1.22	$1.07^{3.22}_{0.42}$	$\Gamma=2.03^{4.23}_{1.07}$	7
63	wabs*mekal	4.21×10^{33}	1.49	$0.42^{1.92}_{0.15}$	$kT=5.40^{41.99}_{1.92}$	8
	wabs*pow	4.37×10^{33}	1.41	$0.58^{1.27}_{0.30}$	$\Gamma=2.02^{3.08}_{1.62}$	8
68	wabs*mekal	1.15×10^{34}	0.81	$0.40^{0.58}_{0.33}$	$kT=4.06^{8.63}_{2.46}$	27
	wabs*pow	1.27×10^{34}	0.78	$0.51^{0.77}_{0.35}$	$\Gamma=2.05^{2.46}_{1.71}$	27
70	wabs*mekal	5.67×10^{33}	0.56	$0.05^{0.19}_{0.00}$	$kT=8.45^{100.00}_{3.43}$	13
	wabs*pow	5.92×10^{33}	0.56	$0.09^{0.27}_{0.00}$	$\Gamma=1.66^{2.24}_{1.22}$	13
71	wabs*pow	5.25×10^{33}	0.34	$0.64^{1.88}_{0.03}$	$\Gamma=1.55^{3.11}_{0.60}$	12
73	wabs*mekal	3.36×10^{33}	0.83	$0.83^{2.01}_{0.25}$	$kT=4.61^{100.00}_{1.08}$	6
	wabs*pow	4.21×10^{33}	0.80	$0.77^{2.83}_{0.27}$	$\Gamma=1.70^{4.27}_{0.78}$	6
76	wabs*mekal	7.83×10^{33}	0.57	$2.39^{5.25}_{1.15}$	$kT=6.74^{100.00}_{1.71}$	12
	wabs*pow	8.54×10^{33}	0.59	$2.47^{6.98}_{0.86}$	$\Gamma=1.79^{3.97}_{0.75}$	12
77	wabs*mekal	1.49×10^{35}	1.42	$0.41^{0.44}_{0.38}$	$kT=1.04^{1.11}_{0.99}$	163
	wabs*pow	1.51×10^{35}	1.75	$0.71^{0.75}_{0.67}$	$\Gamma=3.82^{3.93}_{3.71}$	164
78	wabs*pow	2.55×10^{34}	1.13	$0.36^{0.63}_{0.20}$	$\Gamma=1.01^{1.32}_{0.76}$	29
79	wabs*mekal	5.14×10^{33}	1.45	$0.25^{0.50}_{0.15}$	$kT=1.91^{3.12}_{0.99}$	16
	wabs*pow	5.39×10^{33}	1.27	$0.47^{0.82}_{0.30}$	$\Gamma=2.93^{3.31}_{2.44}$	16

Table 4: X-ray sources previously detected in the NGC 346 field. [HFP2000] numbers are taken from Haberl et al. (2000).

Src	[HFP2000]	RA (2000) *hh mm ss*	DEC (2000) ° ′ ″	Pos. Error ″	Distance ″
1	164	00 56 52.4	−72 12 00	9.8	3.9
3	234	00 57 18.9	−72 25 30	3.4	4.2
5	170	00 57 31.8	−72 13 03	3.6	3.2
9	136	00 57 50.1	−72 07 56	5.1	1.1
13	165	00 58 00.8	−72 12 09	6.3	7.7
14	173	00 58 01.7	−72 13 51	28.2	25.6
20	185	00 58 16.3	−72 16 18	19.0	16.4
24	139	00 58 28.1	−72 08 48	11.0	12.0
28	116	00 58 35.2	−72 03 12	19.4	14.0
68	123	01 00 13.1	−72 04 40	15.9	11.2
77	162	01 00 41.5	−72 11 34	2.3	6.3
78	132	01 01 01.1	−72 06 57	2.8	7.0
79	150	01 01 07.9	−72 10 26	19.0	27.9
81	206	00 56 39.8	−72 20 28	7.4	9.7
82	223	00 57 21.9	−72 23 57	11.6	5.9

Table 5: Photometry of the optical counterparts (WFI data), and distance between the counterpart and the X-ray source. The error quoted in the σ_V column represents the dispersion of the measured data. A σ_V equal to 0.0 thus simply means that only one measure was available. A ':' denotes an uncertain value. If the counterpart is cataloged, the identifier is given in the last column of the Table, together with its spectral type, if known. Identifiers beginning by 'S010202' are taken from the Guide Star Catalog-II.

Src	V (mag)	$B-V$ (mag)	$U-B$ (mag)	$V-R$ (mag)	$R-I$ (mag)	$V-I$ (mag)	σ_V (mag)	dist. (")	Remarks
1	21.32	0.55		0.43	2.14	2.57	0.14	1.6	
2[c]	17.14	0.54		0.53	0.29	0.82	0.02	2.2	S010202097601
4	19.67	−0.01		−0.08	−0.22	−0.30	0.01	0.9	S0102029846
5	18.19	0.50		0.16			0.05	0.9	S01020206684
6	19.55	−0.05	−0.71	−0.14	0.18	0.04	0.07	2.7	
7	18.92:	0.24:	−1.15:	0.59:	0.02:	0.61:	0.36	0.6	
9	15.71	0.01	−0.96	0.10	0.05	0.14	0.01	0.5	[MA93]1038, S010202013449
12	18.86	−0.12	−0.49	0.09			0.09	1.1	S010202012821
13	17.57	−0.04	−0.72	−0.10			0.02	1.8	S0102027728
14[a]	19.11	0.25		0.62	1.46	2.08	0.04	1.3	S01020205791
20	20.70	−0.12		−0.31			0.05	0.2	
24	20.88:	1.28:		1.15:	0.86:	2.01:	0.27	0.7	
26	19.25	−0.16	−0.36	−0.13	1.00	0.87	0.10	0.7	
30	20.05	−0.08		−0.24			0.04	0.1	
32	15.08	0.02	−1.04	0.07	−0.02	0.05	0.01	3.1	[MA93]1104, S01020202934
33	18.71	1.49		0.95	1.37	2.33	0.06	2.5	S010202028457
34	19.41	0.16				0.53	0.08	1.7	
36	12.61	−0.15	−1.07	−0.06	−0.18	−0.24	0.01	0.5	MPG435, O4III(f)
39[a]	19.55	−0.04		−0.28			0.11	2.0	
40	13.59	0.73	0.08	0.31	0.34	0.65	0.01	5.1	AzV218, B1II
41[a]	19.29	0.10	−0.46				0.10	1.7	
42	18.73:	0.80:		0.23:	0.62:	0.85:	0.15	0.6	
43[a]	15.67	−0.21	−0.96	−0.11	−0.20	−0.31	0.01	5.9	S010202020653
44	20.57:	0.73:		−0.76:	2.36:	1.60:	0.42	2.3	
45	19.25	0.81	0.18:	0.50			0.08	1.3	
47	11.32	−0.32	−0.88	0.13	−0.10	0.03	0.01	0.3	HD 5980, LBV
48	15.16	−0.19	−0.97	−0.08	−0.10	−0.18	0.01	7.2	
51[b]	21.24:	0.45:		0.07:	0.16:	0.24:	0.64	0.4	
52	19.42	0.55	0.00	0.46	0.52	0.98	0.07	0.9	
55	19.54	0.87		0.19	0.72	0.91	0.21	1.1	
57	19.42	2.19		0.88	1.67	2.55	0.09	0.9	
59	18.93	−0.13	−0.22	−0.16			0.09	1.6	S01020204530
61[b]	20.41	−0.11	−0.65:				0.13	1.4	
64[b]	20.86	0.25:		0.60	0.38:	0.98:	0.05	1.6	
65	18.08	0.05	0.13	0.08			0.01	1.3	

Table 5: (continued)

67[b]	19.26	0.60	−0.29	0.46			0.10	1.1	[MA93]1240
68[b]	21.32:	1.07:		0.83:	1.08:	1.91:	0.23	1.1	
69[c]	18.87	−0.07		0.42			0.08	1.2	
71[c]	20.82:	0.32:	−3.60:	−0.22:	1.42:	1.20:	0.22	2.0	
72	21.03:						0.39	?	
73	19.55	0.88		0.32			0.09	1.3	
76	16.73	−0.11	−0.84	−0.09	−0.22	−0.31	0.01	2.9	S010202096809
77[d]	17.82	−0.13	−0.68	−0.06	−0.06	−0.12	0.02	1.4	S01020208968
78	15.81	0.00	−0.95	0.08	0.05	0.14	0.02	0.6	S010202016442
79[d]	18.42	0.05		0.24	−0.02	0.23	0.10	2.3	S010202010679

[a] northern component of double
[b] faint
[c] closest within a group
[d] brightest in a group

Table 6: Periods and distance of the optical variable counterparts found in the MACHO database.

Src	Sep. from MACHO source	Period(s)
7	1.34"	4.91d,95d,2380d
14	1.56"	357d
	1.68"	357d
32	2.57"	9.12d
55	1.90"	227d, unusual light curve
76	1.35"	long-term variable
78	1.13"	1316d